



HAL
open science

High-temperature redox chemistry of $\text{La}_{1.5+x}\text{Sr}_{0.5-x}\text{Co}_{0.5}\text{Ni}_{0.5}\text{O}_{4+\delta}$ ($x = 0.0, 0.2$) studied in situ by neutron diffraction

Florent Tonus, Colin Greaves, Hany El Shinawi, T. Hansen, Olivier Hernandez, Peter D. Battle, Mona Bahout

► **To cite this version:**

Florent Tonus, Colin Greaves, Hany El Shinawi, T. Hansen, Olivier Hernandez, et al.. High-temperature redox chemistry of $\text{La}_{1.5+x}\text{Sr}_{0.5-x}\text{Co}_{0.5}\text{Ni}_{0.5}\text{O}_{4+\delta}$ ($x = 0.0, 0.2$) studied in situ by neutron diffraction. *Journal of Materials Chemistry*, 2011, 21 (20), pp.7111-7122. 10.1039/C1JM10445D . hal-00822098

HAL Id: hal-00822098

<https://hal.science/hal-00822098>

Submitted on 14 May 2013

HAL is a multi-disciplinary open access archive for the deposit and dissemination of scientific research documents, whether they are published or not. The documents may come from teaching and research institutions in France or abroad, or from public or private research centers.

L'archive ouverte pluridisciplinaire **HAL**, est destinée au dépôt et à la diffusion de documents scientifiques de niveau recherche, publiés ou non, émanant des établissements d'enseignement et de recherche français ou étrangers, des laboratoires publics ou privés.

High-temperature redox chemistry of $\text{La}_{1.5+x}\text{Sr}_{0.5-x}\text{Co}_{0.5}\text{Ni}_{0.5}\text{O}_{4+\delta}$ ($x = 0.0, 0.2$) studied *in situ* by neutron diffraction†F. Tonus,^a C. Greaves,^{*b} H. El Shinawi,^{‡b} T. Hansen,^c O. Hernandez,^a P. D. Battle^{*d} and M. Bahout^{*a}

Received 28th January 2011, Accepted 9th March 2011

DOI: 10.1039/c1jm10445d

Neutron powder diffraction has been used to investigate the redox behaviour of two $n = 1$ Ruddlesden–Popper (RP) oxides, $\text{La}_{1.5+x}\text{Sr}_{0.5-x}\text{Co}_{0.5}\text{Ni}_{0.5}\text{O}_{4+\delta}$ ($x = 0.0, 0.2$) *in situ* and in real time during cycling through the temperature range $20 < T/^\circ\text{C} < 600$ under flowing 5% H_2 . Both compositions retained $I4/mmm$ symmetry throughout the heating and cooling cycle. Rietveld refinement of data collected at room temperature showed the presence of interstitial oxygen in the original samples ($\delta \approx 0.06(1)$ and $0.12(1)$ for $x = 0.0$ and 0.2 , respectively). When heated in flowing H_2 , both compositions were reduced over the temperature range $300 < T/^\circ\text{C} < 600$ ($\delta \approx -0.22(2)$ and $-0.06(2)$ for $x = 0.0$ and 0.2 , respectively). In the case of the $x = 0.2$ material, reduction clearly occurred first at the interstitial site (O_{int}), then at the equatorial site (O_{eq}). The changes in composition were accompanied by changes in unit-cell parameters and bond lengths. Rietveld refinements revealed residual partial occupation of the O_{int} site in the reduced $x = 0.2$ sample. This is the first structural evidence of the coexistence of both anion vacancies and interstitial anions in a hypostoichiometric $n = 1$ RP oxide. The temperature dependence of the atomic displacement parameters is consistent with the presence of local rotations of the anion-deficient coordination polyhedra. On heating the reduced $x = 0.2$ material in an O_2 flow, the refilling of both the O_{eq} and O_{int} sites began at 200°C and the stoichiometry of the original as-prepared sample was recovered by 250°C .

1. Introduction

The development of mixed ionic–electronic conductors for applications such as solid-oxide fuel-cell (SOFC) electrodes,^{1,2} oxygen separation membranes and catalysts for the partial oxidation of light hydrocarbons³ has relied strongly on the design of perovskite materials $\text{Ln}_{1-x}\text{A}_x\text{BO}_{3-\delta}$ where Ln is a lanthanide, A is an alkaline earth and B is a $3d$ transition metal. Although the conventional cathode materials, $\text{La}_{1-x}\text{Sr}_x\text{MnO}_{3-\delta}$ (LSM) and $\text{La}_{1-x}\text{Sr}_x\text{Co}_{1-y}\text{Fe}_y\text{O}_{3-\delta}$ (LSCF), exhibit interesting ionic and electronic transport properties, they suffer from a number of problems, most notably thermo-mechanical cracking (as a result of thermal expansion mismatching) or chemical instability resulting in the formation of insulating phases when yttria-stabilized zirconia (YSZ) is used as the electrolyte at high operating

temperatures ($\sim 900^\circ\text{C}$). Due to performance and longevity issues associated with high-temperature use, recent research has targeted the development of alternative SOFC cell components working in the intermediate-temperature range, $\sim 700^\circ\text{C}$ (IT-SOFC). With the discovery of electrolyte materials such as lanthanum strontium magnesium gallate $\text{La}_{1-x}\text{Sr}_x\text{Mg}_{1-y}\text{Ga}_y\text{O}_{3-\delta}$ (LSGM) and ceria-doped gadolinia $\text{Ce}_{1-x}\text{Gd}_x\text{O}_{2-\delta}$ (CGO), which have ionic conductivities superior to that of YSZ at intermediate temperatures, it has become necessary to identify alternative cathode materials. It is in this regard that the Ruddlesden–Popper (RP) class of materials,⁴ particularly the La_2NiO_4 -based series that adopt the K_2NiF_4 structure ($n = 1$ RP phases), have attracted significant attention in recent years.^{5–7} The fundamental difference between K_2NiF_4 -type oxides and perovskite oxides, besides their different crystal structures, lies in their defect chemistry; perovskites are commonly oxygen deficient whereas K_2NiF_4 -type oxides can show either oxygen deficiency or oxygen excess. The oxide-ion conductivity in $\text{La}_2\text{NiO}_{4+\delta}$, which is at least one order of magnitude larger than that of conventional perovskites in the IT-range, is a consequence of the high mobility of excess oxygen ions ($\delta > 0$) accommodated in the interstitial sites of the layered structure.^{8–11}

In addition to good mixed ionic–electronic conductivity and electrocatalytic properties, SOFC electrode materials should show chemical and structural stability over the temperature range and under the gas atmosphere associated with the working

^aSciences Chimiques de Rennes, UMR 6226 CNRS-Université Rennes 1, Campus de Beaulieu, Avenue du Général Leclerc, F-35042 Rennes, France. E-mail: mona.bahout@univ-rennes1.fr

^bSchool of Chemistry, University of Birmingham, Edgbaston, Birmingham, B15 2TT, UK

^cInstitut Laue-Langevin, 6, rue Jules Horowitz, F-38000 Grenoble, France

^dInorganic Chemistry Laboratory, University of Oxford, South Parks Road, Oxford, OX1 3QR, UK

† Electronic supplementary information (ESI) available: Supplementary information. See DOI: 10.1039/c1jm10445d

‡ Present address: Chemistry Department, Faculty of Science, Mansoura University, 35516 Mansoura, Egypt.

conditions. *In situ* techniques can play a major role in establishing this stability and they are therefore of growing importance in current materials research. They can provide a deeper insight into the changes that occur when a chemical reaction or physical transformation (*e.g.* a phase transition) occurs within the sample. In particular, solid-state-ionic materials (mainly electrolytes and mixed electronic-ionic materials), in which the removal and insertion of oxygen are important processes, can benefit from investigation by *in situ* neutron powder diffraction (NPD). To date, a few *in situ* high-temperature NPD investigations have been performed on perovskite and K_2NiF_4 -type materials such as $Ln_2NiO_{4+\delta}$ ($Ln = La, Pr, Nd$) in air¹² or under vacuum.^{13,14} However, hitherto studies under H_2 flow, which is the gas atmosphere at the anode side of a conventional SOFC, have only been carried out by our group.^{15,16} Recently, we have studied the K_2NiF_4 -type series $(Ln,Sr)_2Cr_{0.5}M_{0.5}O_{4+\delta}$ ($Ln =$ lanthanide, $M = Ni, Mn$) with the aim of identifying potential SOFC anode materials. *In situ* NPD under flowing H_2 showed that for $M = Ni$ the structure can withstand reducing conditions up to $\sim 700^\circ C$; the oxygen loss from the transition metal layers is accommodated by reduction of Ni^{3+} to Ni^{2+} along with expansion and contraction of the a and c lattice parameters, respectively.^{15,16}

The synthesis of $La_{1.5+x}Sr_{0.5-x}Co_{0.5}Ni_{0.5}O_{4+\delta}$ ($x = 0.0, 0.2$) has been reported recently, together with the structural, transport and magnetic properties. Thermogravimetric analysis under 10% H_2 showed a gradual oxygen loss for the $x = 0.2$ material on heating, whereas a stepwise reduction was observed for the $x = 0.0$ material, yielding at $\sim 400^\circ C$ a $(Co/Ni)^{2+}$ -based composition, $La_{1.5}Sr_{0.5}Co_{0.5}Ni_{0.5}O_{3.74}$, which remains stable under H_2 up to $\sim 800^\circ C$.¹⁷ It has been shown¹⁸ that this material is a good candidate not only for SOFC applications, but also for solid-state electrolysis cells. This adaptability was ascribed to the flexible oxygen stoichiometry of the $n = 1$ structure. The solid/gas reaction of a Co- or Co, Ni-based oxide with H_2 or O_2 and the consequent structural changes have not been studied at high temperature by *in situ* diffraction techniques so far. The reduction of the two compositions $La_{1.5+x}Sr_{0.5-x}Co_{0.5}Ni_{0.5}O_{4+\delta}$ ($x = 0.0, 0.2$) has now been monitored under H_2 flow from $20^\circ C$ up to $\sim 600^\circ C$, using the real-time *in situ* NPD. In addition, the structural evolution of the reduced $x = 0.2$ material has been monitored under O_2 flow in the temperature range 20 – $600^\circ C$, in order to study oxygen intercalation into the available oxygen sites within the K_2NiF_4 structure. The results of these diffraction studies are presented and discussed below.

2. Experimental

The polycrystalline materials $La_{1.5+x}Sr_{0.5-x}Co_{0.5}Ni_{0.5}O_{4+\delta}$ ($x = 0.0, 0.2$) were prepared by solid state reaction as described elsewhere.¹⁷ Neutron diffraction experiments were carried out on the high-flux two-axis neutron powder diffractometer D20¹⁹ at the Institut Laue Langevin (ILL, Grenoble, France) according to the strategy previously described.^{15,16} A take-off angle of 118° from the (117) plane of a germanium monochromator was chosen, giving a wavelength of $\lambda = 1.36 \text{ \AA}$ and a resolution of $\Delta d/d \approx 3 \times 10^{-3}$, while retaining a high flux on the sample ($\sim 10^7 \text{ n cm}^{-2} \text{ s}^{-1}$). Slits were used to define the beam to be 30 mm high and 15 mm wide at the sample position.

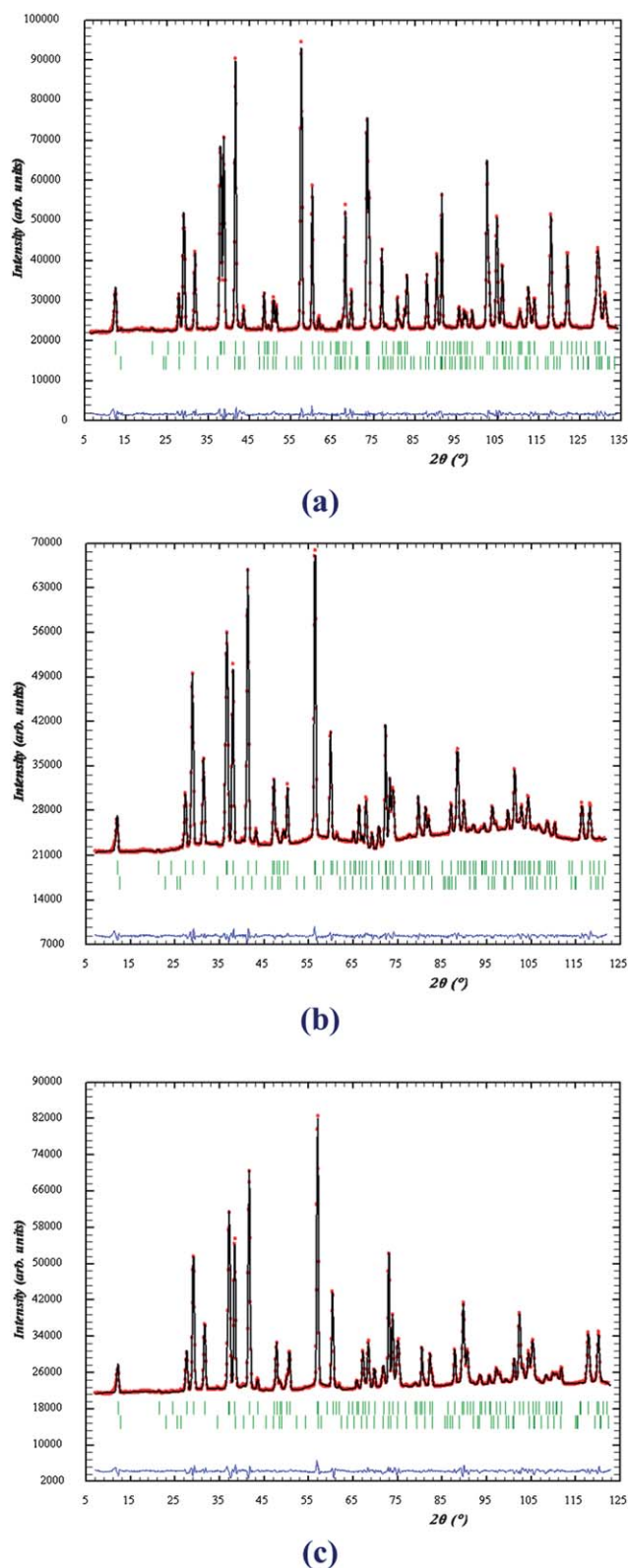


Fig. 1 Rietveld refinements of the neutron powder diffraction patterns of $La_{1.5}Sr_{0.5}Co_{0.5}Ni_{0.5}O_{4+\delta}$ ($x = 0.0$) (a) at $20^\circ C$ before hydrogen reduction, (b) at $600^\circ C$ after reduction, and (c) at $60^\circ C$ after reduction. The lower set of tick marks correspond to a $La(OH)_3$ impurity at $20^\circ C$ and a La_2O_3 impurity at 600 and $60^\circ C$.

Table 1 Structural parameters of $\text{La}_{1.5}\text{Sr}_{0.5}\text{Co}_{0.5}\text{Ni}_{0.5}\text{O}_{4+\delta}$ ($x = 0.0$) derived from neutron diffraction data^a

	Before reduction (20 °C)	After reduction (600 °C)	After reduction (60 °C)
$a/\text{Å}$	3.83605(4)	3.85076(8)	3.82381(8)
$c/\text{Å}$	12.5291(2)	13.0171(4)	12.8335(4)
$V^b/\text{Å}^3$	184.37(1)	193.02(1)	187.64(1)
δ	0.06(1)	-0.22(2)	-0.24(2)
R_{Bragg}	1.26	2.13	2.37
R_{wp}	5.34	5.10	5.80
R_{p}	6.46	7.40	7.66
χ^2	6.60	7.99	19.5
La/Sr	z 0.3620(2)	0.3593(2)	0.3601(2)
	$U_{11} \times 100/\text{Å}^2$ 0.54(6)	2.57(8)	1.40(8)
	$U_{33} \times 100/\text{Å}^2$ 0.38(6)	1.9(2)	1.4(2)
Co/Ni	$U_{11} \times 100/\text{Å}^2$ 0.37(8)	1.5(2)	1.2(2)
	$U_{33} \times 100/\text{Å}^2$ 1.3(2)	3.7(3)	1.6(3)
O_{ax}	Occupancy ^c 1.00	1.00	1.00
	z 0.1702(3)	0.1741(4)	0.1729(4)
	$U_{11} \times 100/\text{Å}^2$ 1.45(6)	4.7(1)	2.5(1)
	$U_{33} \times 100/\text{Å}^2$ 1.3(2)	2.3(2)	1.8(2)
O_{eq}	Occupancy 1.00	0.875(6)	0.868(8)
	$U_{11} \times 100/\text{Å}^2$ 0.6(2)	6.5(3)	4.3(3)
	$U_{22} \times 100/\text{Å}^2$ 0.5(1)	1.3(2)	0.9(2)
	$U_{33} \times 100/\text{Å}^2$ 0.8(2)	3.2(3)	1.3(3)
O_{int}	Occupancy 0.029(5)	0.015(4)	0.013(6)
	$U_{\text{iso}}^d \times 100/\text{Å}^2$ 1.40	3.91	2.29

^a Space group $I4/mmm$. La/Sr on 0 0 z , Co/Ni on 0 0 0, O_{ax} on 0 0 z , O_{eq} on 0 $\frac{1}{2}$ 0, O_{int} on 0 $\frac{1}{2}$ $\frac{1}{4}$. ^b The volume per formula unit. ^c Fixed. ^d Fixed at the U_{eq} value of O_{ax} .

High-temperature measurements under flowing H_2 gas required the modification of the standard sample environment. The powder sample (~ 0.5 g) was loaded in a quartz tube (8 mm diameter) between two pieces of quartz wool which allowed unrestricted gas flow through the sample, while also being the support. The tube was mounted in the standard D20 furnace and connected to a flow of reducing gas (5% H_2/He) which was controlled by a needle valve connected to a Bourdon gauge. The sample position was marked so as to follow any movement during the experiment under the positive pressure of gas; no sample movement was detected once the overpressure range had been determined. The overpressure was set at approximately 200 mbar at room temperature and monitored over the full temperature range to ensure a regular gas flow. The quartz tube was centered in the beam with centering rings top and bottom, and also by a boron nitride collar. In contrast to the previously published data collection¹⁵ where the temperature was calibrated off-beam, in the present experiment two thermocouples were set inside the glass tube just below and over the sample in order to

Table 2 Selected bond lengths (Å) in $\text{La}_{1.5}\text{Sr}_{0.5}\text{Co}_{0.5}\text{Ni}_{0.5}\text{O}_{4+\delta}$ ($x = 0.0$)

	Before reduction (20 °C)	After reduction (600 °C)	After reduction (60 °C)
La/Sr– O_{ax}	2.407(4)	2.413(4)	2.404(4)
	$2.7419(6) \times 4$	$2.7566(6) \times 4$	$2.7363(8) \times 4$
La/Sr– O_{eq}	$2.582(2) \times 4$	$2.658(2) \times 4$	$2.624(2) \times 4$
Co/Ni– O_{ax}	$2.129(4) \times 2$	$2.2628(4) \times 2$	$2.217(4) \times 2$
Co/Ni– O_{eq}	$1.91802(2) \times 4$	$1.92538(4) \times 4$	$1.91191(4) \times 4$
La/Sr– O_{int}	$2.377(1) \times 4$	$2.393(2) \times 4$	$2.377(2) \times 4$
$O_{\text{ax}}-O_{\text{int}}$	$2.165(2) \times 4$	$2.166(2) \times 4$	$2.154(2) \times 4$

control more accurately the temperature of the sample. The furnace element was a 22 mm diameter vanadium-foil cylinder with two further outer vanadium-foil shields (26 and 30 mm diameter) to reduce power consumption and provide a homogeneous temperature environment.

The *in situ* thermal treatment was as follows: with H_2 gas flowing, the samples ($x = 0.0$ and 0.2) were heated up to ~ 600 °C at a heating rate of 1 °C min^{-1} ($x = 0.0$) or 2 °C min^{-1} ($x = 0.2$), and then held at 600 °C for 1 h before being cooled to room temperature at 10 °C min^{-1} . The cooling rate was faster than the heating rate because according to thermal analysis, no change was expected when the sample returns to room temperature.¹⁷ In order to assess the reversibility of the oxygen exchange, the *in situ*-reduced $\text{La}_{1.7}\text{Sr}_{0.3}\text{Co}_{0.5}\text{Ni}_{0.5}\text{O}_{4+\delta}$ ($\delta < 0$) sample was subsequently heated rapidly from RT up to 250 °C under flowing oxygen, held at that temperature for approximately 2 hours and then heated at a rate of 2 °C min^{-1} to ~ 600 °C and held isothermally for 1 h before being cooled to room temperature at a rate of 10 °C min^{-1} . Diffraction patterns were collected in real time throughout the different aforementioned thermal cycles; a data collection took ~ 1 min, giving a maximum temperature resolution of 1 °C. In addition to these time-resolved data, datasets with improved counting statistics were collected from both samples (i) at room temperature just before reduction; (ii) at the upper temperature attained ($T \approx 600$ °C); (iii) after cooling the reduced ($x = 0.0$ and 0.2) and reoxidized ($x = 0.2$) samples to room temperature. For each sample, these data were normalized to a common intensity scale.

In order to ensure a good background correction, a diffraction pattern was collected from the quartz tube and the glass wool support for 1 h at room temperature. This background contribution was then normalized to the incident monitor count so that it could be subtracted from the raw data without introducing significant noise.

All the diffraction patterns were analyzed by Rietveld refinement^{20,21} using the FullProf program.²² The background remaining after subtraction of the instrumental component was treated using a Fourier-filtering technique and the peak profiles were modeled using a Thompson–Cox–Hastings pseudo-Voigt profile function; two asymmetry parameters were refined below $2\theta = 20^\circ$.²³ In order to achieve a satisfactory level of agreement between the observed and calculated diffraction profiles it was necessary to model the anisotropic line broadening that was particularly marked for reflections having a high value of the Miller index l in the data collected from reduced samples. This broadening was accounted for using Stephens' microstructural model;²⁴ four independent anisotropic strain-broadening parameters, S_{hkl} (S_{400} , S_{202} , S_{004} and S_{220}) appropriate for the tetragonal symmetry, were refined. The peak shape did not change significantly during the course of the experiment, indicating that a high level of sample homogeneity was maintained throughout.

3. Results

3.1 Characterization of the as-prepared samples

Although preliminary analysis by X-ray powder diffraction had suggested that the reaction products were monophasic,

Table 3 Structural parameters of $\text{La}_{1.7}\text{Sr}_{0.3}\text{Co}_{0.5}\text{Ni}_{0.5}\text{O}_{4+\delta}$ ($x = 0.2$) derived from neutron diffraction data^a

	Before reduction (43 °C)	After reduction (600 °C)	After reduction (57 °C)	After reoxidation (600 °C)	After reoxidation (58 °C)
$a/\text{Å}$	3.85442(4)	3.87331(6)	3.84881(6)	3.86967(6)	3.85453(4)
$c/\text{Å}$	12.5347(2)	12.8939(4)	12.7032(4)	12.8209(2)	12.5452(2)
$V^b/\text{Å}^3$	186.23(1)	193.44(1)	188.18(1)	191.98(1)	186.39(1)
δ	0.12(1)	-0.06(2)	-0.10(2)	0.11(1)	0.12(2)
R_{Bragg}	1.47	1.65	1.49	1.44	1.13
R_{wp}	4.39	4.75	4.53	4.65	3.92
R_{p}	5.88	7.55	6.49	7.19	5.39
χ^2	5.64	3.56	5.98	5.83	5.97
La/Sr					
z	0.3615(2)	0.3609(2)	0.3618(2)	0.3607(2)	0.3614(2)
$U_{11} \times 100/\text{Å}^2$	0.68(4)	2.22(6)	0.95(6)	1.96(8)	0.79(6)
$U_{33} \times 100/\text{Å}^2$	0.42(6)	1.54(8)	0.87(8)	0.3(1)	0.53(6)
Co/Ni					
$U_{11} \times 100/\text{Å}^2$	0.32(6)	1.12(8)	0.67(8)	0.9(2)	0.40(6)
$U_{33} \times 100/\text{Å}^2$	1.4(2)	3.6(2)	1.7(2)	3.3(4)	1.7(2)
O_{ax}					
Occupancy ^c	1.00	1.00	1.00	1.00	1.00
z	0.1701(4)	0.1765(4)	0.1749(4)	0.1742(4)	0.1701(4)
$U_{11} \times 100/\text{Å}^2$	2.60(6)	4.72(8)	2.35(6)	4.7(2)	2.78(6)
$U_{33} \times 100/\text{Å}^2$	1.6(2)	2.0(2)	1.4(2)	2.3(2)	1.8(2)
O_{eq}					
Occupancy	1.00	0.943(6)	0.931(6)	1.00	0.991(6)
$U_{11} \times 100/\text{Å}^2$	0.7(1)	3.7(2)	1.9(2)	2.4(2)	0.8(1)
$U_{22} \times 100/\text{Å}^2$	0.43(8)	0.9(2)	0.6(1)	0.9(2)	0.4(1)
$U_{33} \times 100/\text{Å}^2$	1.4(2)	3.3(2)	1.2(2)	3.2(2)	1.5(2)
O_{int}					
Occupancy	0.059(4)	0.028(4)	0.018(6)	0.057(4)	0.068(4)
$U_{\text{iso}}^d \times 100/\text{Å}^2$	2.26	3.83	2.05	3.90	2.46

^a Space group $I4/mmm$. La/Sr on $00z$, Co/Ni on 000 , O_{ax} on $00z$, O_{eq} on $0\frac{1}{2}0$, O_{int} on $0\frac{1}{2}\frac{1}{4}$. ^b The volume per formula unit ^c Fixed. ^d Fixed at the U_{eq} value of O_{ax} .

close inspection of the NPD datasets collected at room temperature on both as-prepared materials ($x = 0.0, 0.2$) revealed weak unindexed Bragg reflections attributable to the presence of small amounts of $\text{La}(\text{OH})_3$ (~ 1 mol%) which was

therefore inserted as a second phase in the refinements. This impurity is formed by the reaction with moisture of the very small quantities of La_2O_3 starting material remaining after the synthesis.

Table 4 Selected bond lengths (Å) in $\text{La}_{1.7}\text{Sr}_{0.3}\text{Co}_{0.5}\text{Ni}_{0.5}\text{O}_{4+\delta}$ ($x = 0.2$)

	Before reduction (43 °C)	After reduction (600 °C)	After reduction (57 °C)	After reoxidation (58 °C)
La/Sr– O_{ax}	2.401(4)	2.379(4)	2.377(4)	2.401(4)
	$2.7540(4) \times 4$	$2.7805(6) \times 4$	$2.7607(6) \times 4$	$2.7539(4) \times 4$
La/Sr– O_{eq}	2.594(1) $\times 4$	2.640(2) $\times 4$	2.605(2) $\times 4$	2.596(1) $\times 4$
Co/Ni– O_{ax}	2.131(4) $\times 2$	2.273(4) $\times 2$	2.219(4) $\times 2$	2.133(4) $\times 2$
Co/Ni– O_{eq}	$1.92723(2) \times 4$	$1.93665(3) \times 4$	$1.92440(3) \times 4$	$1.92726(2) \times 4$
La/Sr– O_{int}	$2.3808(8) \times 4$	$2.407(2) \times 4$	$2.392(1) \times 4$	$2.3808(8) \times 4$
$\text{O}_{\text{ax}}-\text{O}_{\text{int}}$	$2.173(2) \times 4$	$2.157(2) \times 4$	$2.149(2) \times 4$	$2.173(2) \times 4$

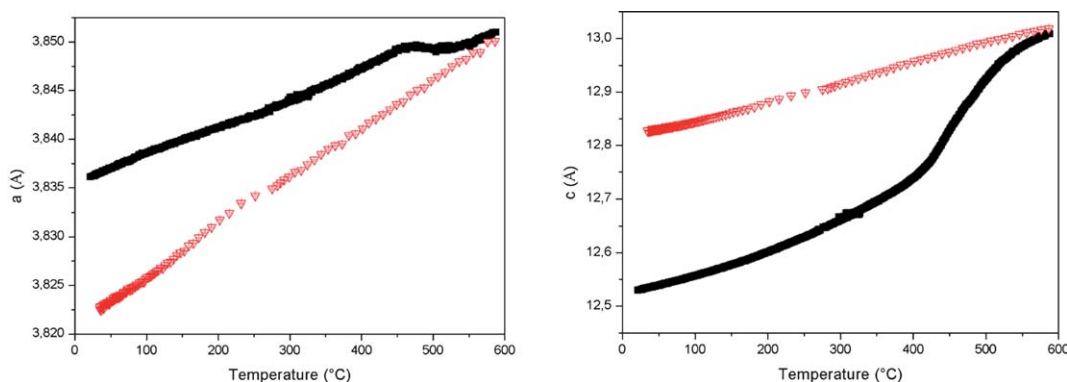


Fig. 2 The temperature dependence of the a and c lattice parameters of $\text{La}_{1.5}\text{Sr}_{0.5}\text{Co}_{0.5}\text{Ni}_{0.5}\text{O}_{4+\delta}$ ($x = 0.0$) from sequential Rietveld refinement of NPD data collected under 5% H_2 -He flow. Black (red) symbols represents data collected on heating (cooling). The estimated standard deviation in these parameters is comparable to the height of the plotted symbol.

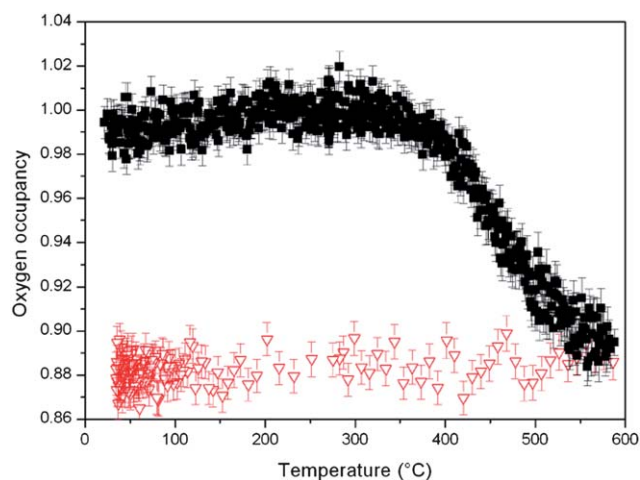
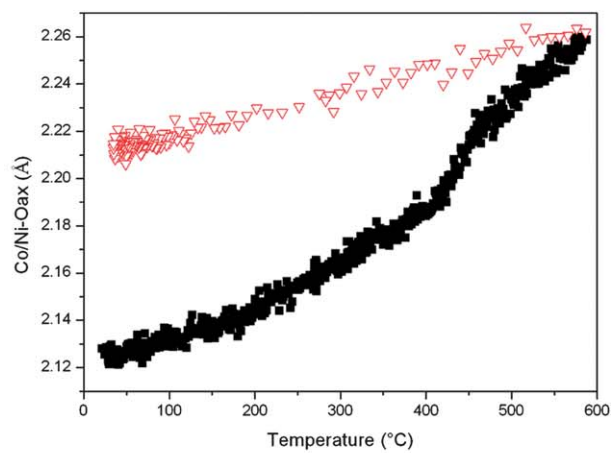


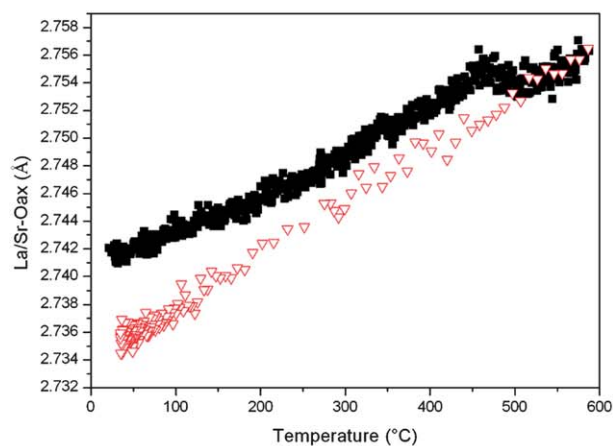
Fig. 3 Occupancy factor of the equatorial oxygen sites in $\text{La}_{1.5}\text{Sr}_{0.5}\text{Co}_{0.5}\text{Ni}_{0.5}\text{O}_{4+\delta}$ ($x = 0.0$) as a function of temperature under hydrogen flow. Black (red) points represent the occupancy of O_{eq} on heating (cooling).

The K_2NiF_4 -like structure was described in the space group $I4/mmm$ with a disordered distribution of La and Sr on a $4e$ site and a disordered distribution of Co and Ni on the $2a$ site. In addition to the oxygen sites, O_{ax} (axial oxygen) at $4e; 0\ 0\ z$ and O_{eq} (equatorial oxygen) at $4c; 0\ \frac{1}{2}\ 0$, an interstitial oxygen site, O_{int} , was included at $4d; 0\ \frac{1}{2}\ \frac{1}{4}$. The displacement parameters of all the atoms (ADP) were refined anisotropically, except for that of O_{int} which was treated as isotropic. Due to strong correlation between the ADP and the occupancy of O_{int} , the former was constrained to equal the equivalent isotropic displacement parameter of the axial oxygen (which proved to be insensitive to the details of the structural model). Our model thus differs from that used in the earlier study of similar compositions.¹⁷ We shall discuss below the consequences of the changes in our refinement strategy. The observed and calculated diffraction patterns are displayed in Fig. 1a and S1a†. The refined structural data are summarized in Tables 1 and 3 and selected bond lengths are given in Tables 2 and 4. A difference Fourier map that is consistent with the inclusion of a partially occupied interstitial anion site in our structural model for the composition $x = 0.0$ is shown in Fig. S2†.

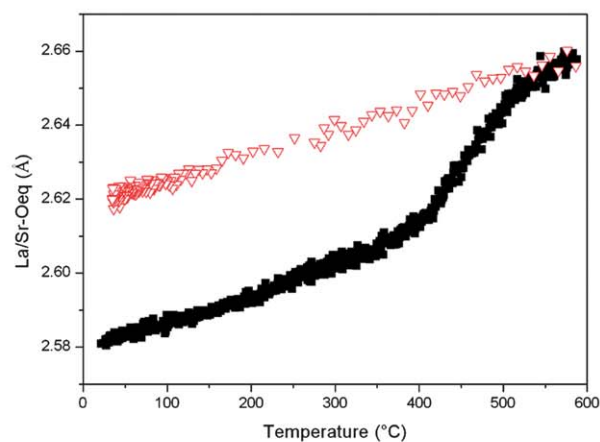
These data have several noteworthy features. Firstly, our refinements showed the presence of interstitial oxygen in both samples, the refined stoichiometries being $\text{La}_{1.5}\text{Sr}_{0.5}\text{Co}_{0.5}\text{Ni}_{0.5}\text{O}_{4.06(1)}$ and $\text{La}_{1.7}\text{Sr}_{0.3}\text{Co}_{0.5}\text{Ni}_{0.5}\text{O}_{4.12(1)}$. This is in reasonable accord with the earlier work on the composition $x = 0.2$, but not with that on $x = 0.0$. However, fresh samples were prepared for this study and it is thus possible for the two nominally $x = 0.0$ samples to have slightly different compositions. The ADPs of the La/Sr and O_{eq} sites in $x = 0.0$ are unremarkable. However, the Co/Ni site has $U_{11} \ll U_{33}$ and O_{ax} has unusually large, but approximately equal, values for the same two parameters. This suggests that O_{ax} is subject to random, static displacements off the ideal position, with the transition metals responding to these displacements. This disorder could be caused by the presence of an oxide ion on a neighbouring interstitial site, and the resulting local $\text{O}_{\text{ax}}\text{--O}_{\text{int}}$ repulsions. However, the ADPs of O_{ax} were also



(a)



(b)



(c)

Fig. 4 Variation with the temperature of the (a) Co/Ni– O_{ax} , (b) La/Sr– O_{ax} and (c) La/Sr– O_{eq} bond lengths in $\text{La}_{1.5}\text{Sr}_{0.5}\text{Co}_{0.5}\text{Ni}_{0.5}\text{O}_{4+\delta}$ ($x = 0.0$). Black (red) symbols represents data collected on heating (cooling) under H_2 flow. The estimated standard deviation in these distances is $0.008\ \text{\AA}$.

enhanced in the sample having $\delta \approx 0$ studied by El Shinawi and Greaves, and so the effect might simply be attributable to disorder on the Co/Ni and, probably more importantly, the La/Sr sublattices whose cations are bonded to O_{ax} . In the case of the composition $x = 0.2$, only the La/Sr site shows unremarkable ADPs. The Co/Ni site again shows signs of displacement along [001] and O_{ax} shows displacements with an enhancement of both the amplitude and the anisotropic character compared to $x = 0.0$. Furthermore, the ADPs of O_{eq} now suggest that it is displaced from the ideal site along [001]. We note that El Shinawi and Greaves previously modelled the anisotropic displacement of O_{ax} in the composition $x = 0.2$ by displacing the atom along [010] whilst retaining an isotropic ADP. Although there are different ways of modeling the structure, the disorder is clearly present in both as-prepared samples at room temperature, and it is more extensive in the composition $x = 0.2$. The model described in Tables 1 and 3 has the advantage that it allows us to model, through the ADPs, displacements of O_{ax} along both [010] and [001]. Further reasons for our choice of model will become apparent when we discuss the analysis of the *in situ* data below.

3.2 *In situ* real-time NPD studies under H_2 flow as a function of temperature

The $x = 0.0$ and 0.2 samples were heated under 5% H_2 flow to 600 °C then held at this temperature for 1 h before being cooled to room temperature. Sequential Rietveld refinements of the NPD data collected *in situ* showed that $I4/mmm$ symmetry was retained throughout the experiment. The data were analysed with the same structural model that was used to describe the as-prepared samples, but with the occupancy factor of O_{eq} added to the list of refined parameters. Preliminary refinements showed that no oxygen was lost from the O_{ax} site under reducing conditions and the occupancy of this site was therefore fixed at unity in our final analyses.

We shall consider first the material with the composition $x = 0.0$. The evolution of the a and c lattice parameters during the experiment (Fig. 2) allows us to identify three different temperature regions in the reduction process: (I) $350 \leq T/^\circ C \leq 450$, (II) $450 \leq T/^\circ C \leq 500$ and (III) $T/^\circ C > 500$. In region (I), both of the lattice parameters show an increase that can be attributed to thermal expansion. In region (II), the value of a remains essentially constant whereas a significant enhancement of c (2.43%) is observed; the rate of expansion is greater than in region (I). In region (III) both a and c increase at a rate comparable to that observed in region (I). Fig. 3 shows the variation of the oxygen occupancy of the equatorial site with temperature during the reduction process. The oxygen loss begins to occur at ~ 350 °C and continues to 550 °C. The occupancy of the interstitial site decreases steadily with increasing temperature, but the data do not allow us to identify a temperature at which the reduction begins. The evolution of the bond lengths, displayed in Fig. 4, shows that the Co/Ni– O_{ax} bond length increases markedly ($\sim 4.0\%$) on heating above 400 °C. The length of the four equivalent La/Sr– O_{ax} bonds decreases between ~ 450 and 550 °C whereas the La/Sr– O_{eq} bond length increases rapidly between ~ 400 and 550 °C. The structural changes are also reflected by the singular behaviour of the anisotropic displacement parameters for O_{eq} , displayed in Fig. 5 for the $x = 0.0$ sample. The

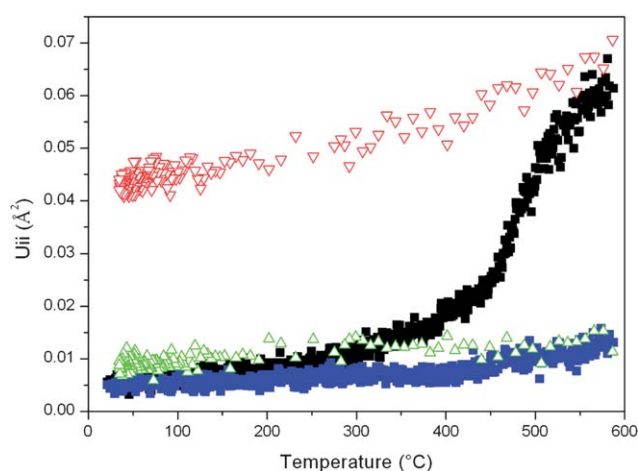


Fig. 5 The temperature dependence of the anisotropic displacements parameter of O_{eq} in $La_{1.5}Sr_{0.5}Co_{0.5}Ni_{0.5}O_{4+\delta}$ ($x = 0.0$) on heating and cooling under 5% H_2 flow; black (red) and blue (green) symbols represent respectively, U_{11} and U_{22} on heating (cooling). The estimated standard deviation in these parameters is $\sim 0.001 \text{ \AA}^2$, comparable to the height of the plotted symbol.

components U_{ii} refined for the original sample at 20 °C do not differ significantly from a spherical shape (Table 1), with values in the range $0.5\text{--}0.8 \times 10^{-2} \text{ \AA}^2$, similar to the isotropic values

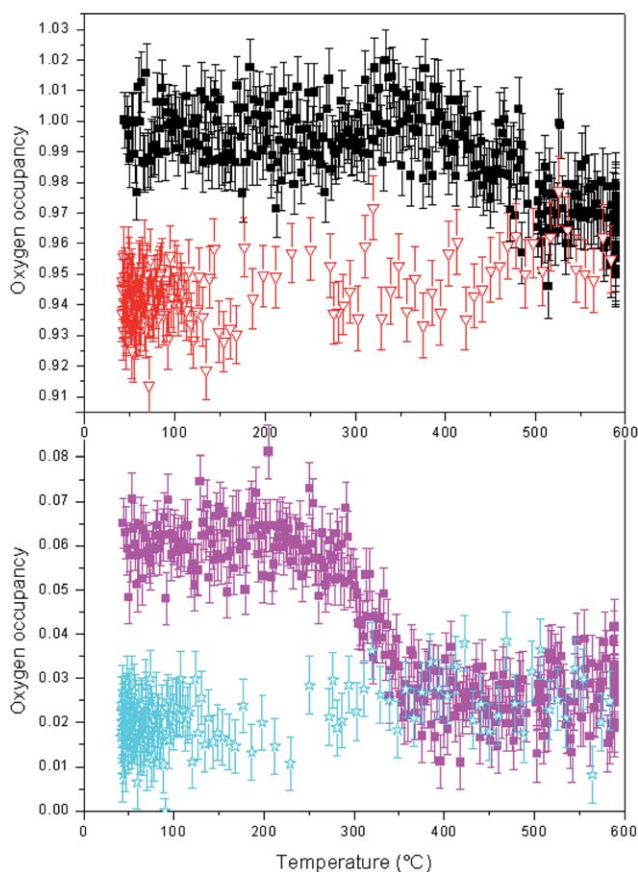


Fig. 6 Occupancy factor of the O_{eq} (top) and O_{int} (bottom) sites in $La_{1.7}Sr_{0.3}Co_{0.5}Ni_{0.5}O_{4+\delta}$ ($x = 0.2$) as a function of temperature under hydrogen flow: for O_{eq} , black (red) symbols represents heating (cooling); for O_{int} , pink (cyan) symbols represents heating (cooling).

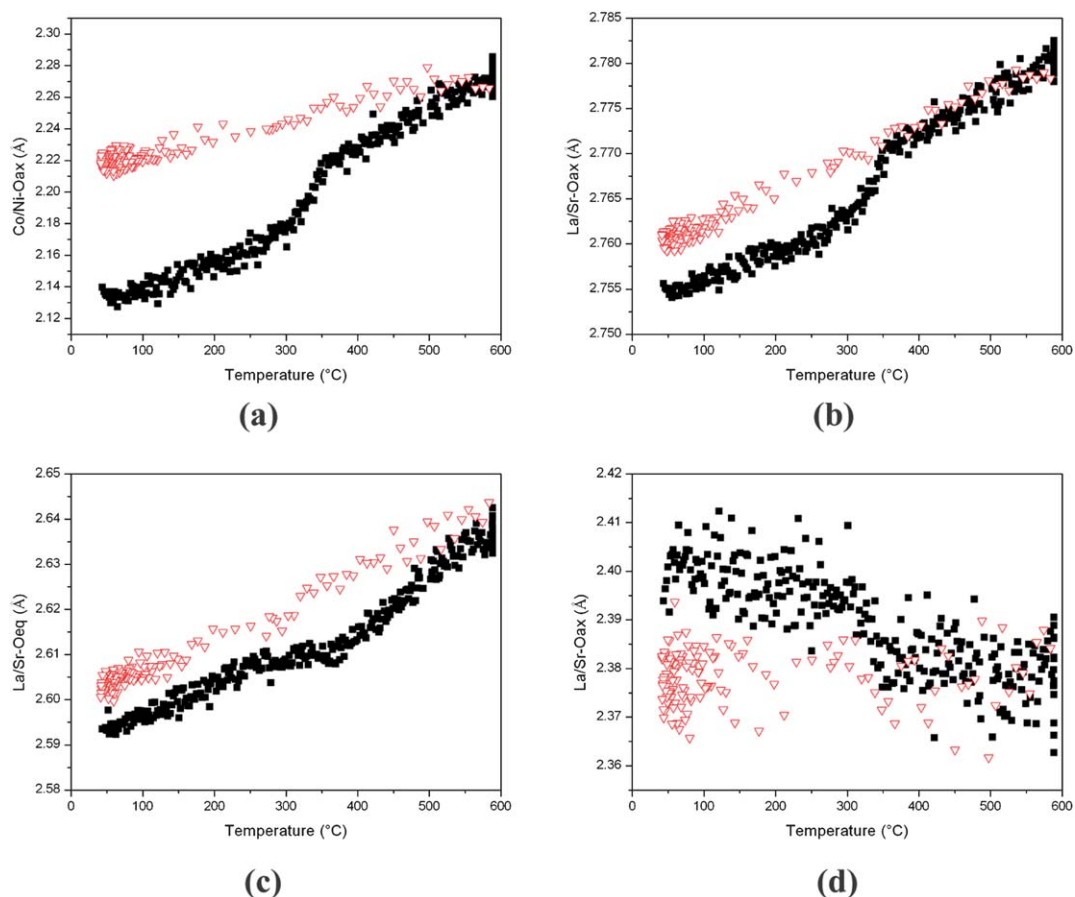


Fig. 7 Variation with the temperature of the (a) Co/Ni–O_{ax}, (b) La/Sr–O_{ax}, (c) La/Sr–O_{eq}, and (d) shortest La/Sr–O_{ax} bond lengths for La_{1.7}Sr_{0.3}Co_{0.5}Ni_{0.5}O_{4+δ} ($x = 0.2$) over a heating/cooling cycle under H₂ flow. Black (red) symbols represent data collected on heating (cooling). The estimated standard deviation in these distances is 0.008 Å.

reported previously ($U_{\text{iso}} \approx 0.8(2) \times 10^{-2} \text{ \AA}^2$ (ref. 17)). However, the structural evolution of the $x = 0.0$ material as a function of temperature under hydrogen flow shows highly anisotropic behaviour; U_{11} (perpendicular to the Co/Ni-bond) increases markedly in comparison to U_{22} (along the bond). The size of U_{11} at 600 °C is ~ 5 times greater than U_{22} and very large by any

standard ($6.5 \times 10^{-2} \text{ \AA}^2$). This implies that there is extensive disorder in a direction perpendicular to the M –O_{eq} bond. When the reduced material is cooled, U_{11} decreases but remains much larger than U_{22} ; for the $x = 0.0$ sample, the values of U_{11} and U_{22} close to room temperature are 4.3×10^{-2} and $0.9 \times 10^{-2} \text{ \AA}^2$, respectively (Table 1). This result indicates the existence of static displacements of O_{eq} in the direction perpendicular to the bond. The previous study of a reduced $x = 0.0$ sample also recognised the presence of anisotropic disorder at the O_{eq} site, but it was modelled by allowing a displacement of the atom to $(x \frac{1}{2} 0)$ and using an isotropic ADP, rather than by using an anisotropic ADP for an atom on the ideal site. This refinement strategy resulted in the values $x = 0.040(2)$ and $U_{\text{iso}} = 0.8(2) \times 10^{-2} \text{ \AA}^2$ at room temperature, with the latter value being similar to that in the original as-prepared sample.¹⁷ This model based on the refinement of the position of O_{eq} could not be used for the sequential treatment of the data collected as a function of temperature in the present study because the refinement became unstable when x was allowed to vary. We shall comment further on the two different approaches in Section 3.3 below.

The structural behavior of the La_{1.7}Sr_{0.3}Co_{0.5}Ni_{0.5}O_{4.12(1)} ($x = 0.2$) material under H₂ flow is different from that of $x = 0.0$. As in the case of the $x = 0.0$ material, our analysis of the structural evolution during the reduction process included refinement of the U_{ii} of O_{eq} at the position $0 \frac{1}{2} 0$. Fig. 6 shows that interstitial

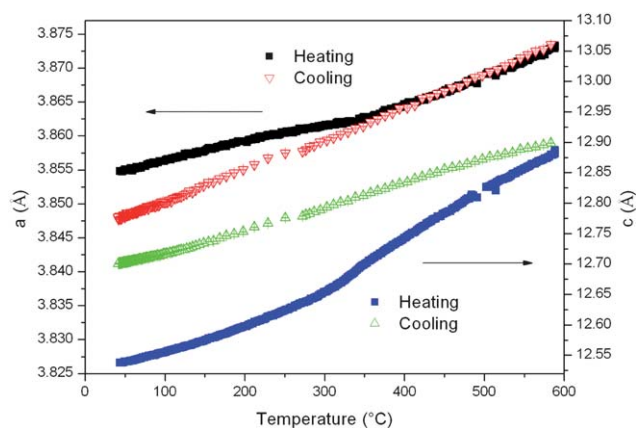


Fig. 8 The temperature dependence of the a and c lattice parameters of La_{1.7}Sr_{0.3}Co_{0.5}Ni_{0.5}O_{4+δ} ($x = 0.2$) upon heating then cooling under H₂ flow. The estimated standard deviation in these parameters is comparable to the height of the plotted symbol.

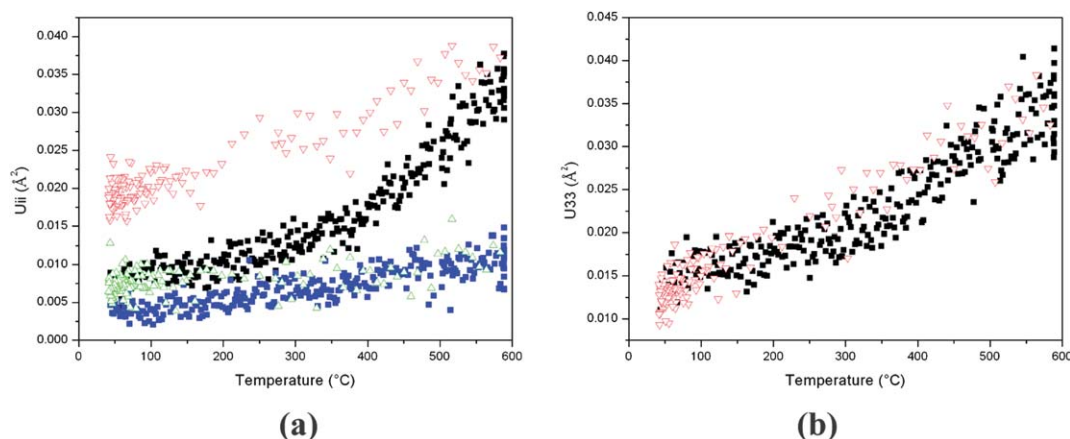


Fig. 9 The temperature dependence of the displacement parameters of O_{eq} under 5% H_2 flow in $La_{1.7}Sr_{0.3}Co_{0.5}Ni_{0.5}O_{4+\delta}$ ($x = 0.2$): (a) black (red) symbols represent U_{11} on heating (cooling), blue (green) symbols represent U_{22} on heating (cooling) and (b) black (red) symbols represent U_{33} on heating (cooling). The estimated standard deviation in these parameters is $\sim 0.001 \text{ \AA}^2$.

oxygen is removed first, in the temperature range 250–350 °C (region I), followed by the removal of equatorial oxygen above $\sim 350 \text{ °C}$ (region II). The main structural changes, as reflected by the evolution of the Co/Ni– O_{ax} , La/Sr– O_{eq} and La/Sr– O_{ax} bond lengths (Fig. 7), occur in region (I), *i.e.* during the loss of O_{int} . The evolution of the a and c parameters exhibits only one change in gradient at $T \approx 330 \text{ °C}$ (Fig. 8). At the same point, U_{11} for O_{eq} begins to increase more rapidly (Fig. 9), suggesting that the anion is displaced perpendicular to the M – O_{eq} bond, as was observed for the $x = 0.0$ material. The ADP of O_{ax} also becomes more anisotropic as the temperature increases, with the displacement perpendicular to the M – O_{ax} bond being significantly larger than that parallel to the bond. As in the case of O_{eq} , the refinements were unstable when this effect was modelled by a displaced isotropic atom, rather than by placing an anisotropic scatterer on the ideal site.

The linear evolution of a and c parameters on cooling the reduced materials (Fig. 2 and 8) confirms the absence of any phase transition. The gradients give similar average thermal expansion coefficients for both samples, ~ 16 to $17 \times 10^{-6} \text{ K}^{-1}$, much greater than those of the as-prepared materials ($8.6 \times 10^{-6} \text{ K}^{-1}$) although the volume expansion of the unit-cell on reduction is different in the two cases; $\Delta V \approx 1.77$ and 1.05% for the $x = 0.0$ and 0.2 samples, respectively. This difference arises in part because different numbers of Co ions are reduced.

3.3 Characterization of the reduced samples

None of the structural parameters provide clear evidence for a change in composition or structure on cooling from 600 to 60 °C; the changes apparent in Fig. 2–9 are all typical of a normal cooling process. The refined stoichiometries of the reduced

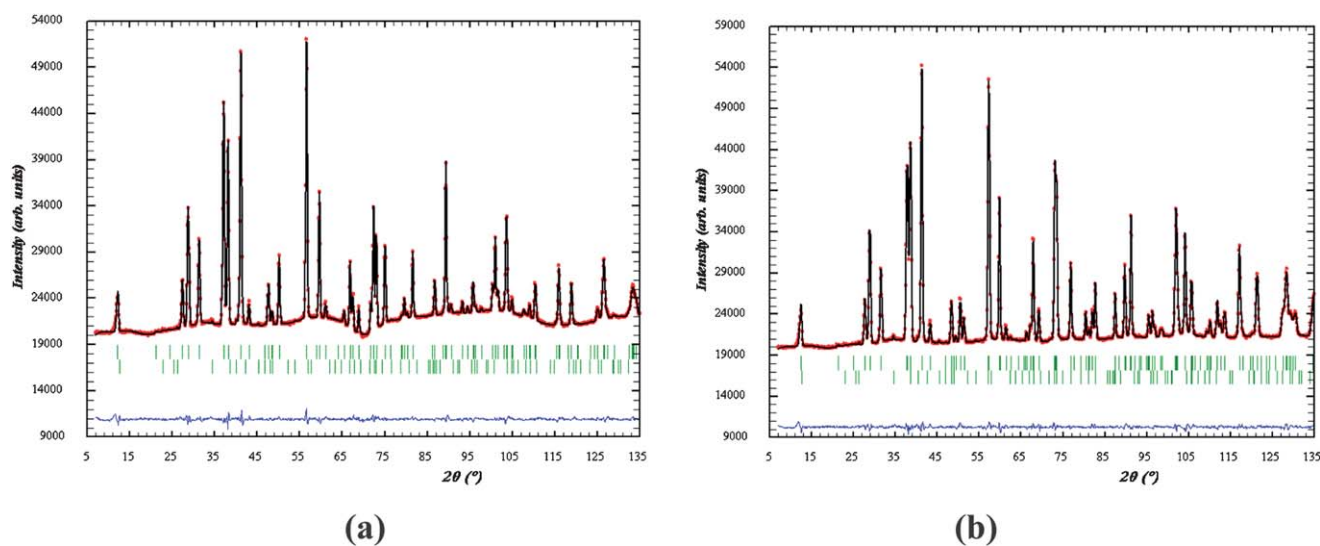


Fig. 10 Two-phase Rietveld refinement of the neutron powder diffraction pattern of $La_{1.7}Sr_{0.3}Co_{0.5}Ni_{0.5}O_{4+\delta}$ ($x = 0.2$) under O_2 flow at (a) 600 °C after heating the reduced material from room temperature (2 °C min^{-1}) and (b) 58 °C after consecutive H_2 - and O_2 -heating/cooling cycles; the lower set of tick marks correspond to a La_2O_3 impurity.

samples, determined at $\sim 60^\circ\text{C}$, are $\text{La}_{1.5}\text{Sr}_{0.5}\text{Co}_{0.5}\text{Ni}_{0.5}\text{O}_{3.78(1)}$ and $\text{La}_{1.7}\text{Sr}_{0.3}\text{Co}_{0.5}\text{Ni}_{0.5}\text{O}_{3.90(1)}$. Fig. S3† and the data in Table 3 suggest that the interstitial oxygen site in the reduced $x = 0.2$ sample is not completely empty, whereas when $x = 0.0$, the residual occupancy of the interstitial site is insignificant. There is no evidence in either case of a lowering of the symmetry of the crystal structure, which would in turn have suggested ordering of the anion vacancies. The thermal ellipsoids at 60°C have similar shapes to those found at 600°C , although they are smaller in size. The retention of relatively large, anisotropic values on cooling shows that the ADPs represent static distortions and not just high-amplitude vibrations. The data collected at 60°C after reduction of the composition $x = 0.2$ give U_{ii} values for O_{ax} which are very similar to those determined at room temperature before reduction. U_{22} and U_{33} of O_{eq} behave in a similar manner. However, the U_{11} parameter of O_{eq} is significantly enhanced in the reduced material. These results are all consistent with the reduction process being centred on the latter site, and they are also consistent with a model in which the transition-metal polyhedra undergo a rotation around [001] when vacancies are introduced onto the O_{eq} site.

3.4 *In situ* reoxidation

The structural and chemical behaviour of the reduced $x = 0.2$ sample was investigated *in situ* under O_2 flow by NPD as a function of temperature. Rietveld plots of the NPD collected at 600°C and after the reoxidized sample was cooled to 58°C are displayed in Fig. 10. The evolution of the oxygen occupancy (Fig. 11) gives evidence of fast and simultaneous oxygen intercalation into both the equatorial and interstitial positions. The reoxidation of the sample is also accompanied by changes in the cell parameters and bond lengths (Fig. 12 and 13) which reverse the changes observed on reduction. The reoxidation began at $\sim 200^\circ\text{C}$ and by the time the temperature had reached 250°C the stoichiometry had returned to that of the original sample. The anisotropic displacement parameter U_{11} of O_{eq} also shows the opposite behaviour to that seen on reduction; it decreases on heating up to the end of the oxygen intercalation at $T \approx 250^\circ\text{C}$, then increases on further heating due to the increase in thermal vibrations (Fig. 14). All the structural parameters (Table 3) and the bond lengths (Table 4) determined at 58°C after reoxidation are in excellent agreement with those determined for the as-prepared sample at 43°C .

4. Discussion

The samples studied in this work all adopt the tetragonal $n = 1$ RP structure. However, the observation of the anisotropic peak broadening shows that the degree of crystallinity is relatively low along [001]. It is surprising to find partial occupation of the interstitial site in the $x = 0.0$ material when the site had previously been found to be vacant in a nominally identical sample. Many aspects of the data presented above merit more detailed consideration. As discussed above, relatively large displacement parameters were found in both studies for the anions on the axial sites of the as-prepared $x = 0.0$ samples. This indicates the presence of local deviations from the average structure which are probably caused by the different

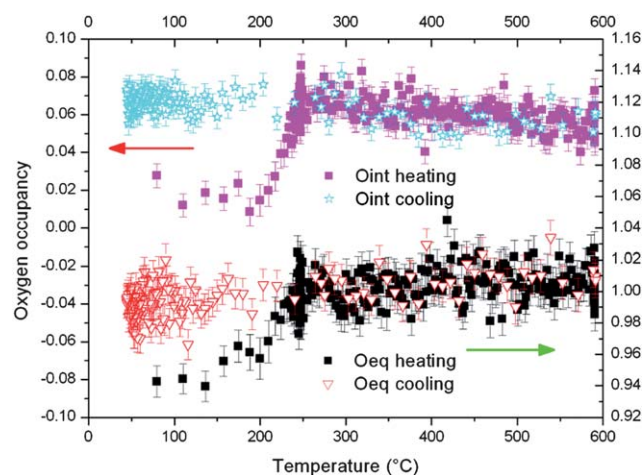


Fig. 11 Occupancy factor of the oxygen sites in $\text{La}_{1.7}\text{Sr}_{0.3}\text{Co}_{0.5}\text{Ni}_{0.5}\text{O}_{4+\delta}$ ($x = 0.2$) as a function of temperature over a reoxidizing cycle under O_2 flow, following a heating/cooling cycle under H_2 flow. Black and pink squares represent the occupancy of O_{eq} (equatorial) and O_{int} (interstitial) sites during heating; red triangles and blue stars represent O_{eq} and O_{int} during cooling.

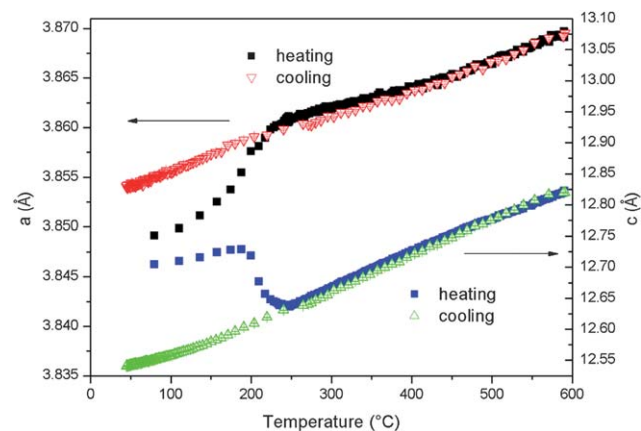


Fig. 12 The temperature dependence of the unit cell parameters a and c of $\text{La}_{1.7}\text{Sr}_{0.3}\text{Co}_{0.5}\text{Ni}_{0.5}\text{O}_{4+\delta}$ ($x = 0.2$) on heating then cooling under O_2 flow, the sample having previously been subjected to a heating/cooling cycle under H_2 flow. The estimated standard deviation in these parameters is comparable to the height of the plotted symbol.

coordination requirements of the Co/Ni and La/Sr cations bonded to these sites. The reduction process involves the removal of oxide ions from the equatorial site, thus reducing the coordination number of the La/Sr site and the Co/Ni site; it also involves reducing the mean oxidation state of the Co/Ni cations from the initial value of $2.5 + \delta$. It can be seen from Fig. 2 that the unit-cell parameters, a and c , show an overall expansion between room temperature and 600°C , but that in the case of the former the removal of oxygen reduces the magnitude of the expansion below the level expected from thermal expansion alone, whereas in the case of the latter it increases it above that level. These deviations from the linear behaviour attributable to thermal expansion alone can be thought of as chemical expansions or contractions that occur when oxygen atoms are removed from the structure. They are

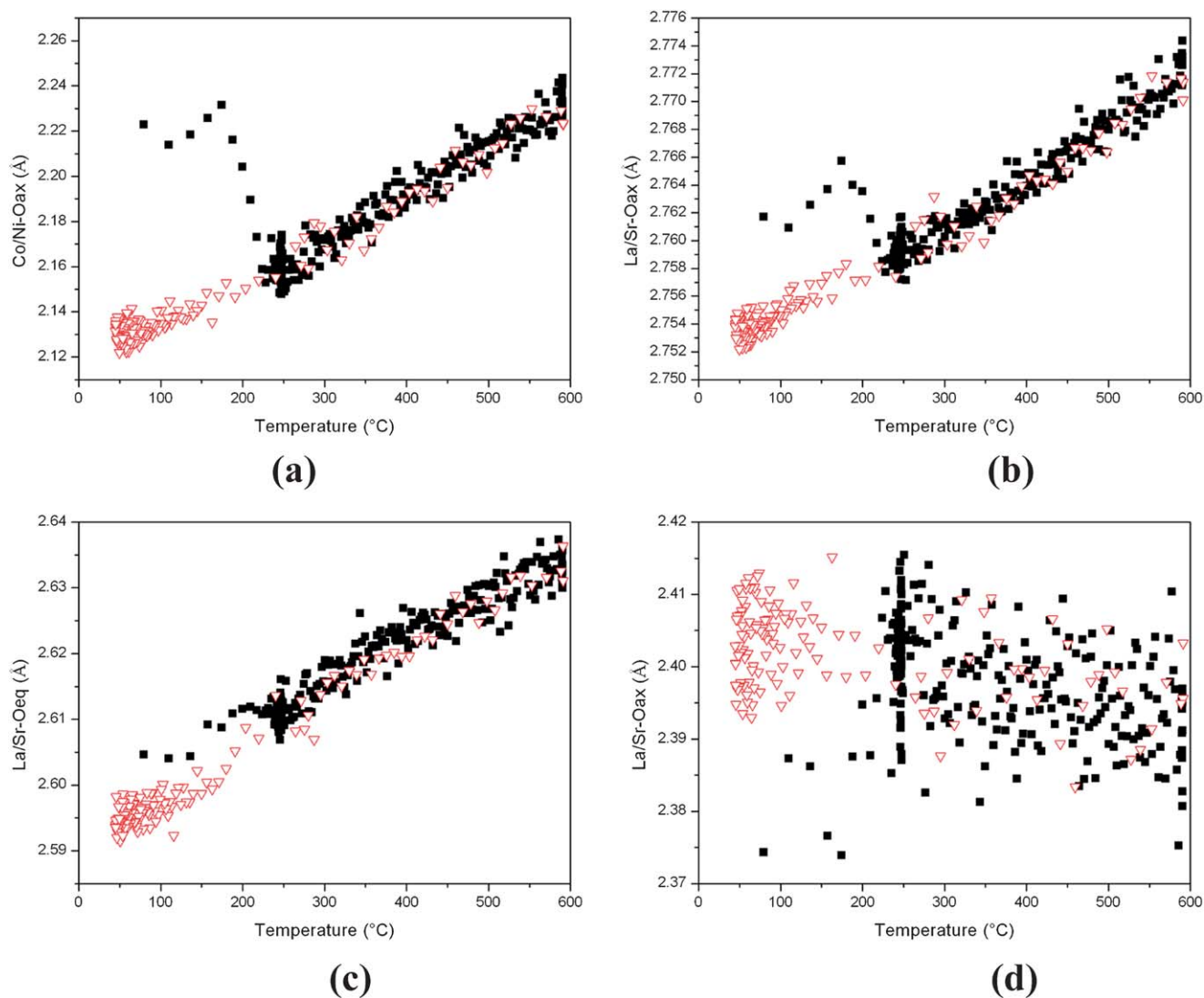


Fig. 13 Evolution with the temperature of (a) $\text{Co/Ni-O}_{\text{ax}}$, (b) $\text{La/Sr-O}_{\text{ax}}$, (c) $\text{La/Sr-O}_{\text{eq}}$, and (d) shortest $\text{La/Sr-O}_{\text{ax}}$ bond lengths for $\text{La}_{1.7}\text{Sr}_{0.3}\text{Co}_{0.5}\text{Ni}_{0.5}\text{O}_{4+\delta}$ ($x = 0.2$) over a heating (black)/cooling (red) cycle under O_2 flow, the sample having previously been subjected to a heating/cooling cycle under H_2 flow. The estimated standard deviation in these distances is 0.008 \AA .

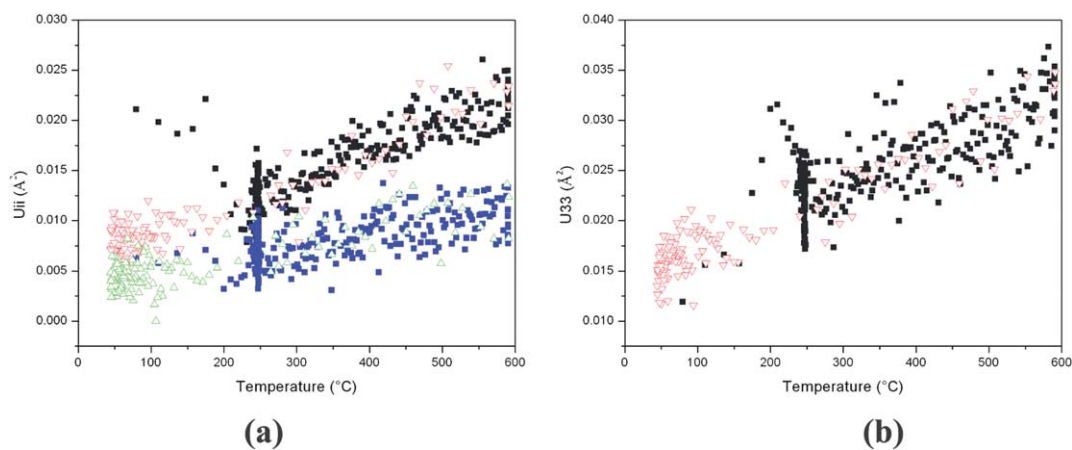


Fig. 14 The temperature dependence of the displacement parameters of O_{eq} under 5% O_2 flow in $\text{La}_{1.7}\text{Sr}_{0.3}\text{Co}_{0.5}\text{Ni}_{0.5}\text{O}_{4+\delta}$ ($x = 0.2$): (a) black (blue) symbols represent U_{11} (U_{22}) on heating, red (green) symbols represent U_{11} (U_{22}) on cooling and (b) black (red) symbols represent U_{33} on heating (cooling). The estimated standard deviation in these parameters is $\sim 0.001 \text{ \AA}^2$.

reflected in the non-linear behaviour of the La/Sr–O and Co/Ni–O bond lengths shown in Fig. 4. The expansion along the *c*-axis affects mainly the perovskite block; the width of the rock-salt layer remains almost constant. The removal of anions from the O_{eq} sites decreases the number of La/Sr–O_{eq} bonds and the La/Sr atoms consequently bond more strongly to the O_{ax} atoms. These bonds lie approximately in the *xy* plane and their strengthening causes the unit-cell parameter *a* to decrease. Fig. 2–5 show that all these changes occur largely over the temperature range 400 < *T*/°C < 500, and that they are clearly interlinked. The reduction of the mean Co/Ni oxidation state is expected to lead to an increase in the mean cation radius and hence to an overall lengthening of the bonds around the transition-metal cations. In order to accommodate the contraction in the *xy* plane required by the La/Sr atoms, this lengthening occurs in an anisotropic manner, with most of the expansion being along [001]. The atomic displacement parameters indicate that significant local disorder is present in the reduced *x* = 0.0 composition. The data in Table 1 and Fig. 5 suggest that O_{eq} undergoes significant displacements perpendicular to the Co/Ni–O_{eq} bond as a result of the reduction process, and that these displacements are still present on cooling to 60 °C. Similarly, O_{ax} is displaced perpendicular to the Co/Ni–O_{ax} bond.

The degree of reduction seen in the present study is slightly lower than that found previously. We assume that the as-prepared sample contains mostly low-spin Co³⁺ and Ni²⁺, with enough Ni³⁺ present to balance the excess negative charge of the interstitial anions. The fully reduced sample is likely to contain mostly high-spin Co²⁺ and Ni²⁺. Consequently we might expect the vacancies to surround Co²⁺ rather than Ni²⁺. XANES experiments are currently being undertaken to test this assumption. Furthermore, we do not know if the vacancies occur in pairs to create four-coordinate cation sites, or whether their distribution is completely random, in which case a mixture of four- and five-coordinate sites will be created. The anisotropic displacement parameters suggest that the polyhedra are rotated away from their original orientation, and that the largest component of the rotation is about the [001] axis. Similar rotations have been observed in the related Co-based materials LaSrCoO_{3.5+δ}²⁵ and (La,Sr)₂Co_{0.5}M_{0.5}O_{4+δ} (*M* = Cr, Mn, Fe)^{26–28} following the reduction of low-spin Co³⁺ to high-spin Co²⁺. In contrast to our approach, the disorder in these materials was modeled by displacing the equatorial oxide ion from (0 1/2 0) to (*x* 1/2 0); the refined *x* value was found to increase with the oxygen deficiency. We note that our results differ in part from those of El Shinawi and Greaves who found *U*₃₃ > *U*₁₁ for O_{ax} in the reduced sample at room temperature. We also note that such marked anisotropy of the *U*_{ii} has not been observed in reduced Co-based *n* = 2 RP phases where oxygen is lost from the axial sites linking the octahedra within the double perovskite layer.^{29,30}

The behaviour of the composition *x* = 0.2 clearly differs from that of *x* = 0.0, principally because of the presence of a higher concentration of anions on the interstitial site. This will lead to stronger O_{int}–O_{ax} repulsions and hence increase the anisotropic nature of the displacements of the oxide ions in the as-prepared sample (Table 3). Fig. 6 shows that oxygen is removed from the interstitial site at a lower temperature than from the O_{eq} site, although the former is not completely emptied. The temperature

dependence of the bond lengths, shown in Fig. 7, is non-linear in the temperature range where only the interstitial anions are being removed. The variation of the bond length with temperature in the region above 400 °C, where only the occupation of the O_{eq} site is decreasing, is essentially the result of linear thermal expansion. The unit-cell parameters (Fig. 8) show a change in their rate of expansion at ~330 °C, within the temperature range where the removal of O_{int} occurs. Although the changes in the bond length appear to be driven by the removal of the interstitial anions, Fig. 9 shows, not surprisingly, that the displacement parameters of O_{eq} increase with temperature more rapidly in the region where that site is being emptied. There is thus a good degree of self-consistency in our analysis. The reduced *x* = 0.2 composition has a higher residual oxygen content than the *x* = 0.0 sample, although the mean oxidation state of the Co/Ni cations is similar (2.1 for the composition determined at 57 °C). The conditions in our *in situ* reduction experiment were clearly not strong enough to induce a mean oxidation state below 2.0, as has been seen previously in the *x* = 0.0 compound¹⁷ and reported in Ni-based related systems.^{31–33} The ADPs after reduction, both at 600 °C and on cooling to 57 °C, show the same anisotropy as was observed in the composition *x* = 0.0 and are again indicative of rotations of the reduced anion polyhedra. The observed range of oxygen stoichiometries corresponds to the presence of both 6- and 5-fold coordination polyhedra, the latter varying from 20 to 40% within the regime where rotation seems likely. However, we cannot rule out the possibility of vacancy pairing leading to the formation of four-coordinate sites.

The reoxidation of the composition *x* = 0.2 is particularly interesting. The structural parameters at 58 °C of the reoxidised sample are in excellent agreement with those determined for the as-prepared sample (Tables 3 and 4). However, the redox chemistry of this material is not reversible because a temperature hysteresis is observed. The O_{int} and O_{eq} sites are repopulated simultaneously between 200 and 250 °C under O₂ whereas under H₂ the removal of O_{eq} begins once the O_{int} site is almost empty.

5. Conclusion

The collection of *in situ* neutron diffraction data on the *n* = 1 Ruddlesden–Popper phases La_{1.5+*x*}Sr_{0.5–*x*}Co_{0.5}Ni_{0.5}O_{4+δ} (*x* = 0.0, 0.2) under flowing H₂ or O₂ as a function of temperature and in real time has enabled us to correlate structural changes with the redox behaviour of these compounds. Most significantly, this experiment has allowed us to monitor for the first time the temperature range and the sequence in which the different oxygen sites (interstitial, axial and equatorial) are emptied and refilled. This information is not available *via* a thermogravimetric analysis or when the diffraction experiments are performed at room temperature on samples that have been reduced *ex situ* and then cooled. Our Rietveld refinements established that the main structural changes that accompany the oxidation and reduction of this material involve the interstitial oxygen site. Furthermore, they revealed the presence of residual anions on the interstitial site in the reduced *x* = 0.2 sample. This is the first structural evidence for the coexistence of both anion vacancies and interstitial oxide ions in an oxygen-deficient *n* = 1 RP oxide. The behaviour of the ADPs suggests that the elongation of the Co/Ni polyhedra along [001]

and the concomitant increase in the anion vacancies in the (Co/Ni)O₂ layers induce a progressive rotation of the Co/Ni polyhedra, principally around the [001] axis. This structural information, when considered together with the results of molecular dynamics calculations, should result in an improved understanding of the oxygen diffusion path in these defect oxides.

Acknowledgements

FT thanks *la Région Bretagne* for financial support. The XRD facilities used for initial characterization were obtained through the Science City Advanced Materials project "Creating and Characterising Next Generation Advanced Materials" with support from Advantage West Midlands (AWM) and part funded by the European Regional Development Fund (ERDF). We are very grateful to A. Daramsy (ILL) for assisting with the collection of the NPD data.

References

- 1 B. C. H. Steele, *Mater. Sci. Eng., B*, 1992, **13**, 79–87.
- 2 Y. Takeda, K. Imayoshi, N. Imanishi, O. Yamamoto and M. Takano, *J. Mater. Chem.*, 1994, **4**, 19–22.
- 3 M. V. Patrakeev, E. N. Naumovich, V. V. Kharton, A. A. Yaremchenko, E. V. Tsipis, P. Núñez and J. R. Frade, *Solid State Ionics*, 2005, **176**, 179–188.
- 4 S. N. Ruddlesden and P. Popper, *Acta Crystallogr.*, 1958, **11**, 54–55.
- 5 A. J. Jacobson, *Chem. Mater.*, 2010, **22**, 660–674.
- 6 A. Tarancon, M. Burriel, J. Santiso, S. J. Skinner and J. A. Kilner, *J. Mater. Chem.*, 2010, **20**, 3799–3813.
- 7 A. Orera and P. R. Slater, *Chem. Mater.*, 2010, **22**, 675–690.
- 8 P. Ganguly and C. N. R. Rao, *Mater. Res. Bull.*, 1973, **8**, 405–412.
- 9 J. M. Bassat, P. Odier and J. P. Loup, *J. Solid State Chem.*, 1994, **110**, 124–135.
- 10 D. Parfitt, A. Chronos, J. A. Kilner and R. W. Grimes, *Phys. Chem. Chem. Phys.*, 2010, **12**, 6834–6836.
- 11 M. Yashima, M. Enoki, T. Wakita, R. Ali, Y. Matsushita, F. Izumi and T. Ishihara, *J. Am. Chem. Soc.*, 2008, **130**, 2762–2763.
- 12 A. Aguadero, J. A. Alonso, M. J. Martínez-Lope, M. T. Fernández-Díaz, M. J. Escudero and L. Daza, *J. Mater. Chem.*, 2006, **16**, 3402–3408.
- 13 S. J. Skinner, *Solid State Sci.*, 2003, **5**, 419–426.
- 14 M. T. Fernández-Díaz, J. L. Martínez and J. Rodríguez-Carvajal, *Solid State Ionics*, 1993, **63–65**, 902–906.
- 15 F. Tonus, M. Bahout, P. D. Battle, T. Hansen, P. F. Henry and T. Roisnel, *J. Mater. Chem.*, 2010, **20**, 4103–4115.
- 16 F. Tonus, M. Bahout, P. F. Henry, S. E. Dutton, T. Roisnel and P. D. Battle, *Chem. Commun.*, 2009, 2556–2558.
- 17 H. El Shinawi and C. Greaves, *J. Mater. Chem.*, 2010, **20**, 504–511.
- 18 M. A. Laguna-Bercero, N. Kinadjan, R. Sayers, H. El Shinawi, C. Greaves and S. J. Skinner, *Fuel Cells*, 2011, **11**, 102–107.
- 19 T. C. Hansen, P. F. Henry, H. E. Fischer, J. Torregrossa and P. Convert, *Meas. Sci. Technol.*, 2008, **19**, 034001.
- 20 L. B. McCusker, R. B. Von Dreele, D. E. Cox, D. Louër and P. Scardi, *J. Appl. Crystallogr.*, 1999, **32**, 36–50.
- 21 H. M. Rietveld, *J. Appl. Crystallogr.*, 1969, **2**, 65–71.
- 22 J. Rodríguez-Carvajal, *Phys. Rev. B: Condens. Matter Mater. Phys.*, 1993, **192**, 55–69.
- 23 J.-F. Berar and G. Baldinozzi, *J. Appl. Crystallogr.*, 1993, **26**, 128–129.
- 24 P. W. Stephens, *J. Appl. Crystallogr.*, 1999, **32**, 281–289.
- 25 M. A. Hayward and M. J. Rosseinsky, *Chem. Mater.*, 2000, **12**, 2182–2195.
- 26 H. El Shinawi and C. Greaves, *Z. Anorg. Allg. Chem.*, 2009, **635**, 1856–1862.
- 27 H. El Shinawi, J. F. Marco, F. J. Berry and C. Greaves, *J. Solid State Chem.*, 2009, **182**, 2261–2268.
- 28 H. El Shinawi and C. Greaves, *J. Solid State Chem.*, 2008, **181**, 2705–2712.
- 29 S. E. Dann and M. T. Weller, *J. Solid State Chem.*, 1995, **115**, 499–507.
- 30 H. El Shinawi, A. Bertha, J. Hadermann, T. Herranz, B. Santos, J. F. Marco, F. J. Berry and C. Greaves, *J. Solid State Chem.*, 2010, **183**, 1347–1353.
- 31 M. Crespin, J. M. Bassat, P. Odier, P. Mouron and J. Choisnet, *J. Solid State Chem.*, 1990, **84**, 165–170.
- 32 M. Crespin, C. Landron, P. Odier, J. M. Bassat, P. Mouron and J. Choisnet, *J. Solid State Chem.*, 1992, **100**, 281–291.
- 33 J. E. Millburn and M. J. Rosseinsky, *Chem. Mater.*, 1997, **9**, 511–522.